Materials Horizons

ROYAL SOCIETY OF CHEMISTRY

COMMUNICATION

View Article Online
View Journal | View Issue

Check for updates

Cite this: *Mater. Horiz.*, 2024, **11**, 3892

Received 30th January 2024,
Accepted 20th May 2024

DOI: 10.1039/d4mh00111g

rsc.li/materials-horizons

Treasure-bowl style bifunctional site in cerium–tungsten hetero-clusters for superior solar-driven hydrogen production†

Pengliang Sun,‡[a,c] Eduardo Gracia-Espino, ‡[b] Fang Tan,‡[a,c] Hua Zhang,[a,c] Qingquan Kong,[d] Guangzhi Hu *[a,c] and Thomas Wågberg *[b,e]

Electrochemical water splitting powered by renewable energy sources hold potential for clean hydrogen production. However, there is still persistent challenges such as low solar-to-hydrogen conversion efficiency and sluggish oxygen evolution reactions. Here, we address the poor kinetics by studying and strengthening the coupling between Ce and W, and concurrently establishing Ce–W bi-atomic clusters on P,N-doped carbon (WN/WC–CeO$_{2-x}$@PNC) with a "treasure-bowl" style. The bifunctional active sites are established using a novel and effective self-sacrificial strategy involving *in situ* induced defect formation. In addition, by altering the coupling of the W(d)–N(p) and W(d)–Ce(f) orbitals in the WN/WC–CeO$_{2-x}$ supramolecular clusters, we are able to disrupt the linear relationship between the binding energies of reaction intermediates, a key to obtain high catalytic performance for transition metals. Through the confinement of the WN/WC–CeO$_{2-x}$ composite hetero-clusters within the sub-nanometre spaces of hollow nano-bowl-shaped carbon reactors, a stable and efficient hydrogen production *via* water electrolysis could be achieved. When assembled together with a solar GaAs triple junction solar cell, a solar-to-hydrogen conversion efficiency of 18.92% in alkaline media could be realized. We show that the key to establish noble metal free catalysts with high efficiency lies in the fine-tuning of the metal–metal interface, forming regions with near optimal adsorption energies for the reaction intermediates participating in water electrolysis.

New concepts

Single-cluster site catalysts with uniform metal active sites have tremendous potential in classical catalytic reactions. However, research on the introduction of oxygen vacancy defects into hetero-clusters to enhance the electronic structure for solar-driven water splitting remains unreported. Here, we propose a novel and effective self-sacrificial *in situ* induced defect strategy using phosphotungstic acid supramolecular clusters. This strategy demonstrates excellent electrochemical performance and solar-to-hydrogen conversion efficiency. The synergistic effect at the Ce–W bi-atomic clusters not only lowers the adsorption energy of reaction intermediates but also facilitates electronic rearrangement, effectively tuning local conductivity, and charge density, thereby enhancing catalytic activity. The single-cluster site catalyst unveils a path for renewable fuel production towards a carbon-free green energy generation.

Introduction

Hydrogen is considered an ideal green-energy carrier for zero-emission technologies.[1] Electrocatalytic water splitting driven by renewable energy with zero carbon emissions is considered an efficient, environmentally friendly, and promising pathway for large-scale production of clean hydrogen fuel to alleviate the global energy and environmental crises.[2–4] Solar-driven water splitting can be divided into photoelectrochemical (PEC) and electrocatalytic water splitting.[5,6] Despite extensive studies on PEC water splitting, its industrial-scale applications are limited by inherent shortcomings such as low light-trapping ability, limited selection of semiconductor materials, and severe photocorrosion.[7,8] Solar-driven water splitting, on the other hand, can effectively produce hydrogen and can be integrated with existing industrial systems to realize the conversion of solar energy to chemical energy.[9,10] Yet, the slow kinetics of electrochemical water splitting pose a significant energy barrier in alkaline media. Consequently, this process demands a cell voltage well beyond the theoretical value of 1.23 V to surmount the activation energy barrier and facilitate water decomposition at an acceptable rate.[11] Efficient catalysts are key components

---

[a] *Donghai Laboratory, Zhoushan 316021, China. E-mail: guangzhihu@ynu.edu.cn*
[b] *Department of Physics, Umeå University, Umeå S-90187, Sweden. E-mail: thomas.wagberg@umu.se*
[c] *Institute for Ecological Research and Pollution Control of Plateau Lakes, School of Ecology and Environmental Science, Yunnan University, Kunming 650504, China*
[d] *School of Mechanical Engineering, Chengdu University, Chengdu 610106, China*
[e] *Wallenberg Initiative Material Science for Sustainability, Department of Physics, Umeå University, Umeå S-901 87, Sweden*

† Electronic supplementary information (ESI) available. See DOI: **https://doi.org/10.1039/d4mh00111g**

‡ These authors contributed equally.

in the electrolyser to lower the activation energy of the water splitting. In alkaline media, non-noble metal are more feasible but are still outcompeted in efficiency and stability by scarce and expensive Pt-group metals and their oxides. Novel combinations and alloys of certain transition metals have however shown impressive progress in efficiency in recent years.

Among these, tungsten-based electrocatalysts are strong candidates to catalyse the OER and HER because of their abundancy, their environmentally benign properties, and high intrinsic catalytic activity.[12] It has been reported that transition metal carbides (TMCs) (TaC,[13] Mo_2C,[9] and WC[14]) and transition metal nitrides (TMN) (MoN,[15] Mo_2N_3,[16] and W_2N[12]) have attractive attributes with metal-like physicochemical properties and well-adapted electronic structures. Here, we note that the d-band electronic structure of WC[14] is similar to that of Pt near the Fermi levels (E_F), which potentially provides for a swift H_{ads} release, one of the descriptive parameters of an efficient HER. Sun *et al.*[17] reported a catalytic electrode based on a N-doped WC nanoarray. They could show that N-doping optimises the hydrogen bonding by adjusting the surface energy levels, thus kinetically accelerating the reaction. However, this effect is limited to acidic systems and the underlying mechanism remains unclear. Other studies taking advantage of the similarity of W-based nitrides and precious metals (Pd and Pt) when interacting with hydrogen atoms, was reported by Fu *et al.*[18] who synthesized WN on RGO using $H_3[PO_4(W_3O_9)_4]$ anion clusters as the W source. They showed that the interaction of P with RGO and WN increased the work function, close to that of Pt metal. The surface work function has been shown to correlate well with the metal–hydrogen bond strength[16,19] and the hydrogen adsorption energy weakens linearly with an increased work function.[20–22] It is thus clear that doping or hybridisation can optimise the W–H_{ad} bond to promote the adsorption of hydrogen and desorption of H_{ad}, further improving the HER performance,.[23] However, whether water dissociation or OH_{ad} desorption can be promoted on the surface of tungsten nitride in alkaline HER remains unclear. An interesting strategy to facilitate both adsorption/dissociation and hydrogen adsorption is to establish heterostructures where the two different surfaces can form heterojunctions that can accelerate the hydrogen diffusion step by and promote the subsequent Heyrovsky step.[24]

Cluster catalysts represent an interesting form of materials where the redox states can be affected compared to their bulk surface counterparts,[25] and thereby optimise the adsorption/dissociation of water and the formation of H*/OH* intermediates. They can also serve as model systems making it possible to get insight into structure/compositional effects on water splitting mechanisms. However, so far most metal nitrides and carbides have been synthesized as nanoparticles with no corresponding cluster structure. Constructing fully exposed nanoclusters remains however challenging because in a reaction system, the metal/non-metallic elements usually form separate phases.

Herein, we utilize a simultaneous carbonisation of different metals in a limited space to form a variety of hetero-element dopants, resulting in a three-dimensional (3D) porous electrocatalyst comprising nitrogen- and phosphorus-doped bowl-shaped carbon encapsulating WN/WC–CeO_{2-x} hetero-clusters. We find that, when used for water splitting reactions in alkaline media, the 3D open porous structure of WN/WC–CeO_{2-x} allows for a good mass transfer and gas evolution while maintaining a stable solid–liquid interface. High-density heterogeneous metal clusters provide an abundance of active sites, while the bowl structure facilitates the diffusion of reactants. Moreover, the interconnected bowl-shaped carbon improves the conductivity and structural stability of the encapsulated nanoclusters during electrocatalysis. DFT calculations reveal that oxygen vacancies in cerium oxide weaken the adsorbed interaction between metal species and enable f–d orbital coupling through the entry of the Ce atoms into the surface of W, which results in suitable binding energies for the H-intermediates to efficiently generate H_2. A solar-driven water electrolyser employing the electrocatalyst achieves a stable, sustainable green hydrogen production with a solar-to-hydrogen (STH) conversion efficiency of 18.92%. Our study presents a viable strategy for designing fully exposed nanocluster catalysts for advancing the field of electrocatalytic water splitting.

Results and discussion

Structural model

The interfacial properties of tungsten nitride (WN)–tungsten carbide (WC) with oxygen vacancy-defective cerium oxide (CeO_{2-x}) were investigated using first-principles computational methods. The initial cells were constructed for crystalline WN(001), WC(100) and CeO_{2-x}(111); their respective parameters are presented in Table S1 (ESI†). The CeO_{2-x}(111) surface featuring oxygen vacancy (O_v) defects was aligned with WN(001)/WC(100) along the [100] direction (Fig. 1(a)), forming a highly symmetric and minimally lattice-mismatched WN(001)/WC(100)–CeO_{2-x}(111) hetero-superlattice. The optimised configuration of WN/WC–CeO_{2-x} remained stable, showing no structural changes or bond disruptions (Fig. S1, ESI†), confirming the compatibility of WN(001)/WC(100) with CeO_{2-x}(111). Thus, coherent interface engineering between WN/WC and CeO_{2-x} is feasible. The characteristics of the WN(001)/WC(100)–CeO_{2-x}(111) interface were evaluated by constructing a three-dimensional charge density difference profile (Fig. 1(b)), demonstrating electron accumulation at the apex of the interface within the CeO_{2-x} domain, stemming from enhanced electron transfer from W to Ce proximal to the interface, which promotes electron donation from WN/WC to CeO_{2-x}. Such heterostructuring intensifies the electronic interactions between WN/WC and CeO_{2-x}, consequently influencing the energetics at the interface. The surface energy of WN/WC–CeO_{2-x} (0.04 eV Å^{-3}) exceeds that of WN/WC (0.01 eV Å^{-3}) (Fig. S2, ESI†). The calculated interfacial energy of WN/WC–CeO_{2-x} was -1.013×10^4 eV Å^{-3}, indicating that heterostructure formation is exothermic, thereby facilitating favourable binding interactions.[12] Electronic localisation functions (ELF) were computed to delineate the electronic local distribution within the WN/WC–CeO_{2-x} hetero-clusters (Fig. 1(c)). ELF analysis of the (010) plane of the WN/WC–CeO_{2-x} supercell demonstrated clear electron

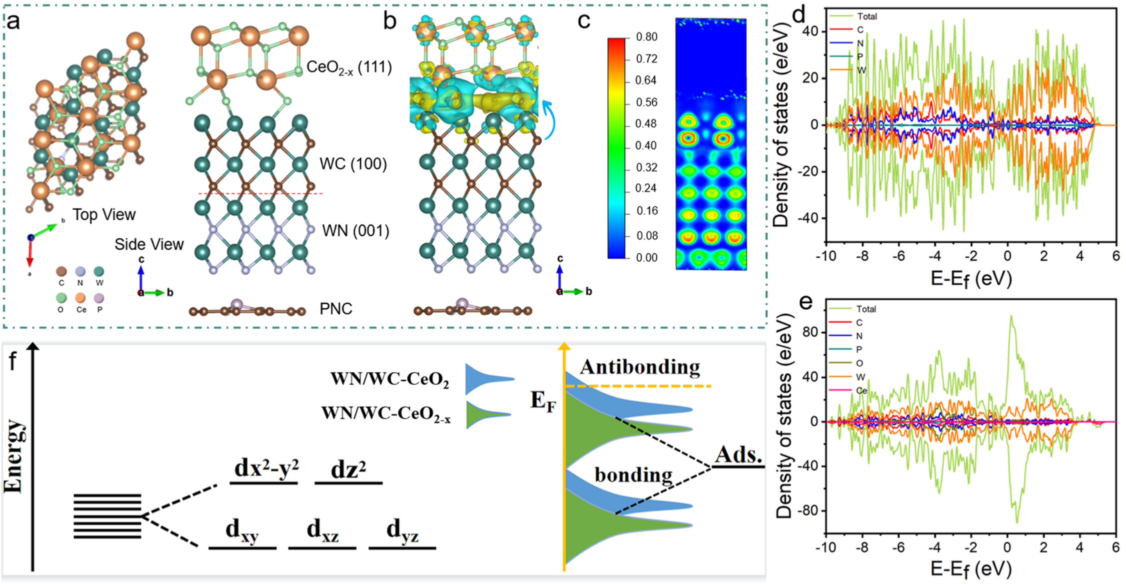

Fig. 1 DFT analysis. (a) Schematic of lattice matching between WN(001)/WC(100) and CeO_{2-x}(111). (b) Distribution of charge density difference at WN/WC and CeO_{2-x} interface. (c) ELF across the interface as shown in panel (b) of WN(001)/WC(100) and CeO_{2-x}(111) hetero-clusters. DOS of (d) WN/WC@PNC and (e) WN/WC–CeO_{2-x}@PNC. (f) Corresponding antibonding and bonding interactions.

accumulation around Ce and W,[14] highlighting the ability of the WN/WC clusters to redistribute charge in the vicinity of the Ce–W centres, thereby acting as pivotal mediators in promoting the electrocatalytic activity of WN/WC–CeO_{2-x}.

The projected density of states (PDOS) (Fig. 1(d) and (e)) was computed to analyse the electronic properties of WN/WC–CeO_{2-x}. Compared to WN/WC and WN/WC–CeO_2 (Fig. S3, ESI†), the introduction of oxygen vacancies, (V_o) and Ce induced a pronounced distribution of W states near the Fermi level in WN/WC–CeO_{2-x}, accompanied by a higher density of metallic states, indicating enhanced electron transfer at the interface of WN/WC–CeO_{2-x}. The d-band centre (ε_d) is an important indicator of the bonding stability and strength of catalytic intermediates.[26] The broader d-band and higher ε_d in proximity to the Fermi level in WN/WC–CeO_{2-x} (Fig. S4, ESI†) indicate increased occupancy of the antibonding orbitals, which favours the adsorption of reaction intermediates, consequently accelerating the reaction. The ε_d of WN/WC–CeO_2 and WN/WC–CeO_{2-x} maintained distinct offsets relative to E_f, with values of −2.339 and −2.357 eV, respectively (Fig. S4, ESI†). The oxygen vacancies induce disparities between the d-band centres of Ce and W active sites, consequently lowering the free energy of the rate-determining step (RDS). Coupling WN/WC with V_o-defective CeO_{2-x} created additional active sites and enhanced the conductivity, facilitating efficient charge transfer during catalysis. The coupling also modulates the electronic structure of the Ce–W species, which lowers the formation energy barrier for reaction intermediates (Fig. 1(f)). This fine-tuning of the electronic structure enhances the intrinsic activity of the resulting electrode and further improves its catalytic performance.

Synthesis and structural characterization

Guided by the theoretical calculations, silica microspheres was coated with dopamine, phosphotungstic acid anion clusters, cerium salt, and resorcinol–formaldehyde polymer using a one-pot method *via* a template polymerization method (Fig. 2(a)). Subsequently, through a simple solvothermal reaction, the precursors were polymerised by electrostatic attraction and metal ion coordination,[9,16] and finally the formation of uniformly dispersed nanoclusters was promoted by pyrolysis. The clusters in the nanopores show higher stability and less tendency to agglomerate during heat treatment, which can greatly improve the utilisation of metals. Utilizing a one-step pyrolysis approach of polyoxometalates within confined spaces, this study achieved simultaneous collection of multiple elements and facilitated doping of diverse elements. This innovative strategy resulted in the formation of monodisperse clusters anchored within porous carbon bowls, enabling efficient hydrogen production *via* water electrolysis.

The surface morphology of WN/WC–CeO_{2-x}@PNC was characterized using field emission-scanning electron microscope (FE-SEM). The WN/WC–CeO_{2-x} hetero-clusters are uniformly distributed on the bowl-shaped carbon (Fig. 2(b)); and SEM of the samples during synthesis (Fig. S5, ESI†). Transmission electron microscope (TEM) imaging shows that the WN/WC–CeO_{2-x} were uniformly confined in the pores of the bowl-shaped carbon matrix (Fig. 2(c)). The corresponding intensity changes in the high-angle annular dark field-scanning transmission electron microscopy (HAADF-STEM) images of WN/WC–CeO_{2-x}@PNC confirmed the formation of a mixture of alloy nanocrystals (Fig. S6, ESI†) and fully exposed single clusters (Fig. 2(d)). Isolated single clusters (marked by red circles in Fig. 2(d)) were clearly visible on the entire support. The HAADF-STEM images of the nanocrystals agglomerated into clusters showed lattice spacings of 0.176, 0.198, and 0.306 nm, corresponding to the distances between the WN(001), WC(100), and CeO_2(311) faces, respectively (Fig. S6, ESI†). The HAADF-STEM

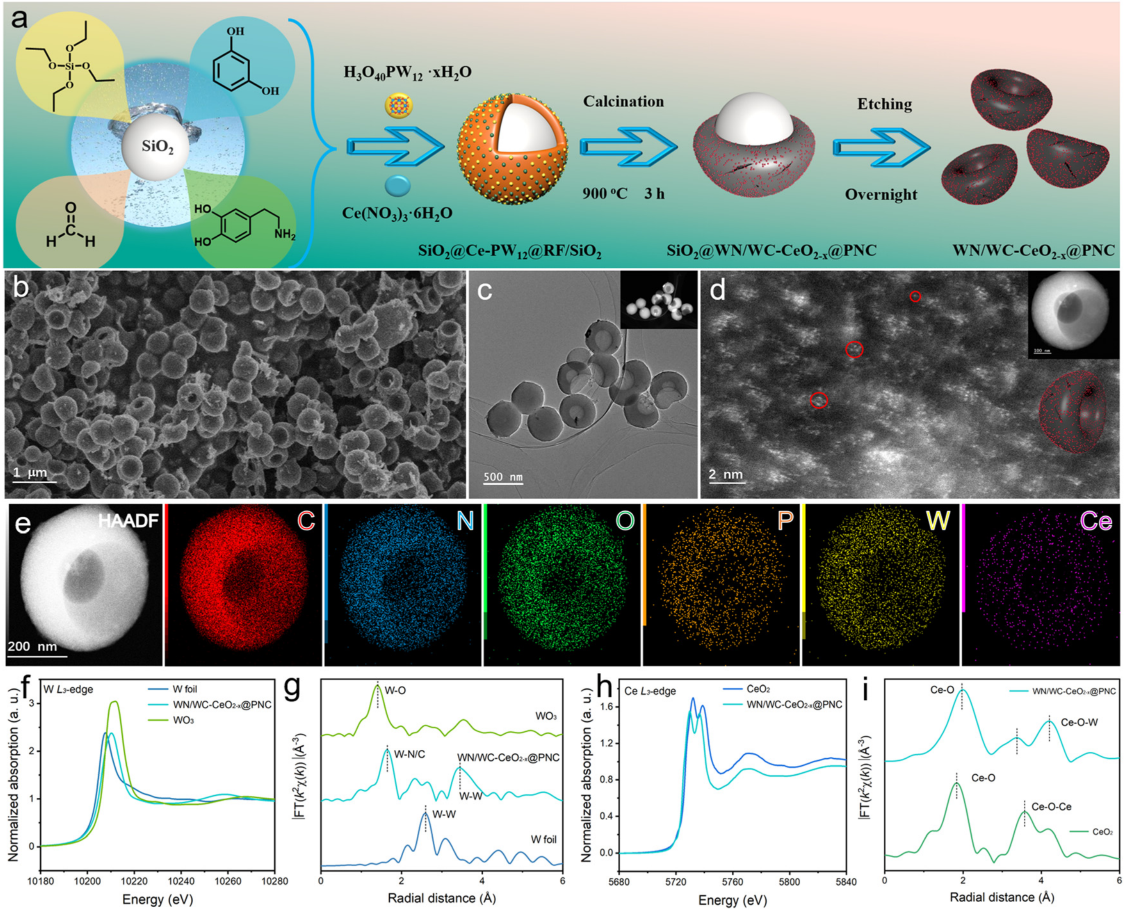

Fig. 2 Structural characterization of the treasure-bowl shaped electrocatalysts. (a) Synthesis schematic of WN/WC–CeO_{2-x}@PNC catalysts. (b) SEM image of WN/WC–CeO_{2-x}@PNC. (c) HRTEM image of WN/WC–CeO_{2-x}@PNC. (d) AC-HAADF-STEM image of WN/WC–CeO_{2-x}@PNC. Monodispersed CeO_2–WN/WC clusters are denoted by red circles. (e) HAADF-STEM image, and corresponding EDX elemental mappings of C, N, O, P, W, and Ce for WN/WC–CeO_{2-x}@PNC. (f) W L_3-edge and (h) Ce L_3-edge XANES spectra of WN/WC–CeO_{2-x}@PNC, and the reference samples; EXAFS spectra of (g) W L_3-edge; (i) Ce L_3-edge in the *R*-space of WN/WC–CeO_{2-x}@PNC and the reference samples.

image of WN/WC–CeO_{2-x}@PNC and the corresponding EDS elemental map (Fig. 2(e)) show that Ce, W, O, N, and P were uniformly distributed on the bowl-shaped carbon. Doping with different heteroatoms can induce, strain, and structural defects in carbon materials,[27] and may alter the charge density of the carbon materials,[28] thereby potentially improving overall water splitting kinetics.

The normalized X-ray absorption near edge structure (XANES) and the Fourier-transformed extended X-ray absorption fine structure (EXAFS) spectra of W L_3-edge and Ce L_3-edge were measured to explore the local electron or atomic structure of WN/WC–CeO_{2-x}@PNC. In Fig. 2(f), the W L_3-edge threshold E_0 of WN/WC–CeO_{2-x}@PNC is situated between that of standard W foil and WO_3, indicating an average oxidation state of tungsten ranging between 0 and +6. Fig. 2(g) provides a more detailed insight into the local chemical coordination of tungsten sites within the sample. Here, the reference sample W foil exhibits a prominent peak at ∼2.58 Å (W–W), while commercial WO_3 powder shows a primary peak at ∼1.42 Å (W–O). Notably, WN/WC–CeO_{2-x}@PNC displays a main peak at ∼1.63 Å, indicative of the presence of a W–N/C environment. To further validate the aforementioned atomic coordination, Ce L_3-edge XAFS and XANES analyses were conducted. As depicted in Fig. 2(i), the scattering paths of the Ce center in WN/WC–CeO_{2-x}@PNC within the *R* space exhibit a prominent peak associated with Ce–O coordination at ∼1.98 Å. Furthermore, by analyzing the Ce L_3-edge XANES spectra presented in Fig. 2(h), the absorption threshold positions for WN/WC–CeO_{2-x}@PNC and pure CeO_2 were determined. The slight reduction in the Ce valence of WN/WC–CeO_{2-x}@PNC indicates further electron redistribution characteristics upon the introduction of tungsten.

The powder X-ray diffraction (XRD) pattern of the WN/WC–CeO_{2-x}@PNC sample (Fig. 3(a)) exhibited several characteristic peaks that matched well with several standard cards. The XRD peaks were consistent with WN (JCPDS no. 89-5266), WC (JCPDS no. 51-0939), and hexagonal close-packed CeO_2 (JCPDS no. 81-0792). The wide diffraction peak at 23.5° corresponds to the (002) crystal plane of carbon. Note that the heteroatom-doped graphite-like carbon ensures that the WN/WC–CeO_{2-x} hetero-clusters are wrapped on the hierarchical bowl carbon substrate, which simultaneously improves the intrinsic activity, reaction kinetics, and structural stability of the composite.[29]

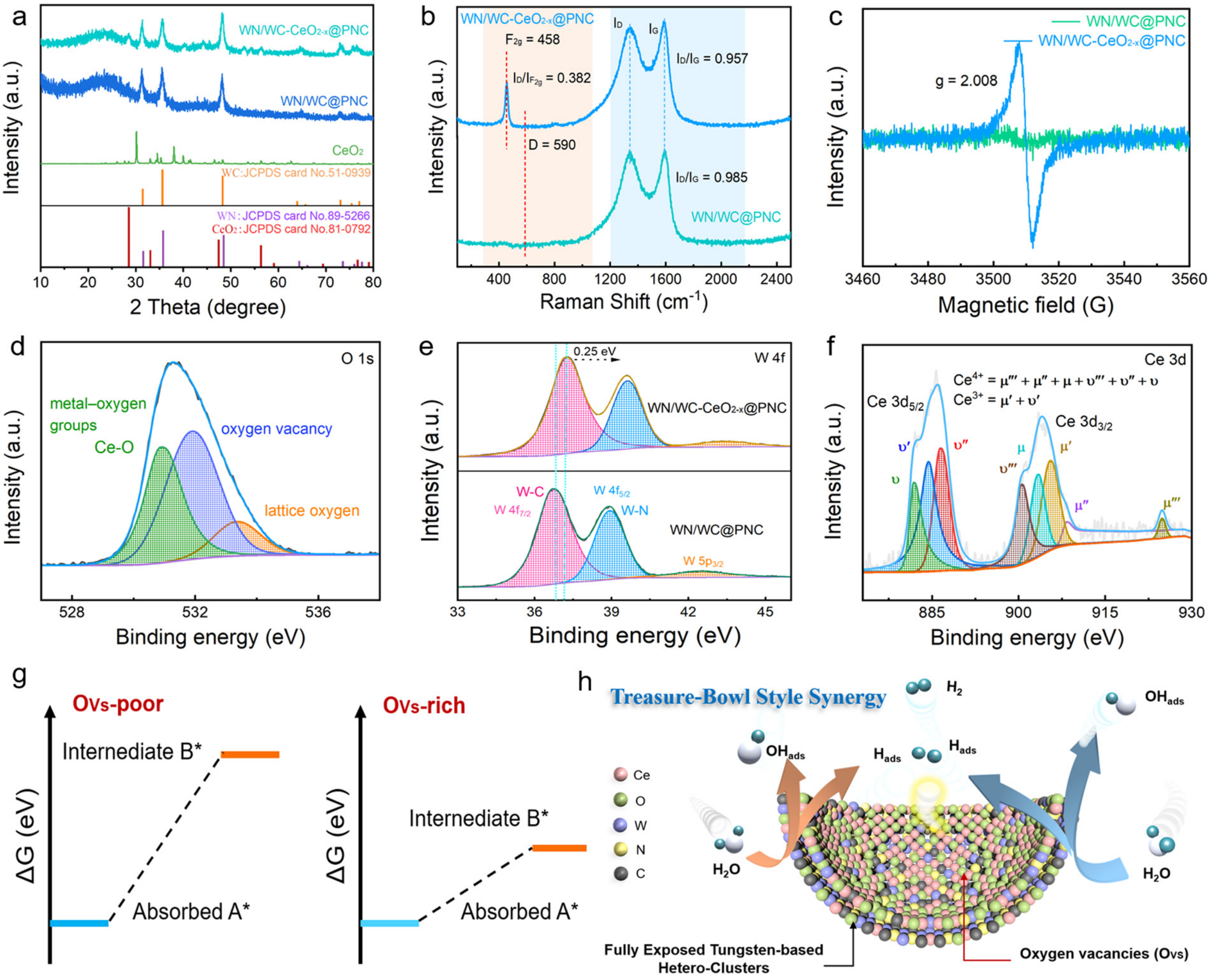

Fig. 3 Structural analysis of WN/WC–CeO_{2-x}@PNC. (a) XRD patterns, (b) Raman spectra, (c) EPR spectrum of WN/WC–CeO_{2-x}@PNC and WN/WC@PNC. XPS survey spectra and high-resolution (d) O 1s, (e) W 3f, and (f) Ce 3d XPS profiles of WN/WC–CeO_{2-x}@PNC. (g) surface reaction on electrocatalyst with and without O_{Vs}. (h) Schematic of the HER steps in basic medium of "Treasure Bowl" type hetero-cluster.

The concentration of bulk oxygen vacancies (O_{Vs}) and surface structure of the catalyst were studied by Raman spectroscopy. The Raman spectrum of the WN/WC–CeO_{2-x}@PNC (Fig. 3(b)) showed a strong peak near 458 cm^{-1} and a weak band around 590 cm^{-1}, corresponding to the typical F_{2g} symmetrical vibration (O–Ce–O extension) and defect induced vibration mode (D band, especially oxygen defect-induced band) of CeO_2 with a cubic fluorite structure, respectively.[30] The wavenumber difference between the oxygen defect and F_{2g} bands is $\sim$130 cm^{-1}, which indicates that the O_{Vs} of the WN/WC–CeO_{2-x}@PNC catalyst is caused by intrinsic defects ($Ce^{4+} \rightarrow Ce^{3+}$).[31] However, the transferred electrons are easily trapped in the O_{Vs}, and the electron paramagnetic resonance (EPR) spectrum of WN/WC–CeO_{2-x}@PNC shows a strong signal at g = 2.008 (Fig. 3(c)), which also confirms the defect structure of the oxygen vacancy. It is generally believed that the strength ratio between defect-induced vibration mode and F_{2g} mode (*i.e.* $I_D/I_{F_{2g}}$) is proportional to the concentration of O_V in CeO_2-based materials.[32] Therefore, we further use the relative ratio of defect band to F_{2g} signal to indicate the concentration of oxygen vacancy. The intensity ratio ($I_D/I_{F_{2g}}$ = 0.382) of the WN/WC–CeO_{2-x}@PNC catalyst (Fig. 3(b)) was significantly higher than that of WN/WC@PNC (without the characteristic peak of O_{Vs}), indicating that the enhanced deformation of the Ce–O–W interface significantly promotes the formation of surrounding defects. Moreover, the oxygen vacancies shorten the electron transfer path and improve the efficiency of charge separation and transfer, thus accelerating the kinetics of the HER.[33] As presented in Fig. 3(b), the D-band (1342.5 cm^{-1}) and G-band (1590.0 cm^{-1}) come from the defect/disorder-induced sp^3 carbon and the sp^2 hybrid carbon with hexagonal bond in the graphite network, respectively.[33] The relative intensity ratio (I_D/I_G) of these two bands is usually used to estimate the degree of graphitization. A smaller I_D/I_G indicates a higher degree of graphitization of carbon materials.[34] For WN/WC–CeO_{2-x}@PNC, I_D/I_G = 0.957, indicating a high degree of graphitization, suggesting good electrical conductivity. Studies have shown that there are large number of defects in graphitized carbon, which may be the potential active centers of electrocatalysis.[35] Additionally, the highly graphitized carbon also makes a great contribution to the long-term durability of electrocatalyst because of its stronger oxidation resistance at high potentials.[36]

The adsorption–desorption isotherm of WN/WC–CeO_{2-x}@PNC was classified as type IV with an obvious hysteresis in the relative pressure (P/P_0) range of 0.5–1.0, indicating mesoporous characteristics and a high Brunauer–Emmett–Teller (BET) specific surface area, which are beneficial for exposing the active sites in the electrocatalytic process (Fig. S7 and Table S2, ESI†). The material was grown using fully exposed WN/WC–CeO_{2-x} hetero-clusters on 3D porous bowl-shaped carbon. Based on our findings, we suggest that the 3D bowl structure is favorable for capturing various reactants and rapidly releasing H_2/O_2 products from the electrolyte (Fig. S8, ESI†), exposing more active sites, reducing the energy barrier for intermediate formation, and improving the kinetics of the overall water splitting reaction. This is supported by the modified electronic structure (N and P doping), good electronic conductivity, and a bowl structure rich in active sites, which are necessary for realising multifunctional electrocatalysis, rapid electron transfer, and efficient mass transfer.

The catalytically active surface species of WN/WC–CeO_{2-x}@PNC were analysed using X-ray photoelectron spectroscopy (XPS). The C 1s spectrum was deconvoluted into three main peaks at 284.4, 285.0, and 288.3 eV, corresponding to the C–C, C–N, C–O, and C═O groups, respectively (Fig. S9a, ESI†). The peaks of W–N, pyridine N, pyrrole N, and graphite N were observed at 398.0, 398.8, 399.6, and 401.3 eV, respectively, in the N 1s spectrum (Fig. S9b, ESI†). The apparent W–N binding energy peak (398.5 eV) in the N 1s spectrum of WN/WC–CeO_{2-x}@PNC, typical of metal nitrides, confirmed the effective modification of the electronic structure of the carbon materials, which facilitates interaction between the heteroatoms and metals.[37–39] The water splitting process is further promoted by the combination of pyridine and pyrrole N, and the formation of oxygen intermediates.[40] The O 1s spectrum shows signals of metal–oxygen groups (Ce–O), oxygen vacancies, and lattice oxygen at 530.7, 531.3, and 532.0 eV, respectively (Fig. 3(d)). The P 2p spectrum (Fig. S9c, ESI†) was deconvoluted into peaks at 130.0 and 129.2 eV, ascribed to P $2p_{1/2}$ and P $2p_{3/2}$, respectively. The peak near 35.5 eV in the W 2p XPS profile of WN/WC–CeO_{2-x}@PNC was divided into two peaks (Fig. 3(e)) at 36.5 eV (W–N) and 34.5 eV (W–C). The peak for WN/WC–CeO_{2-x}@PNC was positively shifted by ~0.25 eV compared to that of WN/WC@PNC, indicating that the coupling between WN/WC and CeO_2 changed the chemical composition and charge on the WN/WC surface, that is, the transfer of electrons from the WN/WC surface to the CeO_2 surface. The mixed valence state of Ce in WN/WC–CeO_{2-x}@PNC was revealed in the high-resolution Ce 3d XPS profile (Fig. 3(f)). The rapid redox/oxidation cycle of Ce^{3+} and Ce^{4+} in CeO_2 facilitates the loss of oxygen or electrons from CeO_2 to form oxygen vacancies or defects, and the valence state and defect structure of CeO_2 are dynamic, making it easier to form favourable active sites for catalysis.[41] Among them, the binding energy of Ce $3d_{5/2}$ and Ce $3d_{3/2}$ at 886.1 and 904.7 eV can be attributed to the Ce^{3+} of $3d^{10}4f^1$ electronic configuration in CeO_x, while the other two peaks at 882.1 and 900.7 eV can be attributed to Ce^{4+} in CeO_2.

It is well known that oxygen vacancies are ubiquitous on the surface of the samples, which can adjust the electronic structure, crystal structure and surface chemistry of the catalyst, thus affecting its conductivity, charge transfer kinetics, and the number of active sites and adsorption/desorption free energy. In total these parameters strongly affect the catalytic activity for HER and OER.[42] We speculate that the coordinated unsaturated metal atoms around the O_{Vs} can effectively trap and activate the reactants as tentatively shown in Fig. 3(g). Here, a "treasure bowl" type hetero-cluster was designed, where individual active clusters are isolated on the "treasure bowl" (Fig. 3(h)). The synergy of O_{Vs} defects would allow movement within their respective "bowls", while migration across "bowls" is obstructed, achieving the dynamic constraint design of single clusters.

Electrochemical active site modulation

The unique bowl-shaped structure and dispersed clusters of WN/WC–CeO_{2-x}@PNC are expected to greatly promote the production and availability of active sites, resulting in high potential for electrocatalytic applications. To test this hypothesis, the HER activity of WN/WC–CeO_{2-x}@PNC was evaluated using a typical three-electrode system with 1.0 M KOH, and a commercial Pt/C with the same load as benchmark. The linear sweep voltammetry (LSV) curves of various catalysts with iR compensation were recorded at a scanning rate of 5 mV s^{-1} (Fig. 4(a)). Specifically, WN/WC–CeO_{2-x}@PNC exhibited an overpotential of 68.6 mV at a current density of 10 mA cm^{-2}, which is significantly lower than that of WN/WC@PNC (142.1 mV), PNC (352.3 mV, Fig. S10, ESI†), and CeO_2 (319.4 mV). The overpotential of WN/WC–CeO_{2-x}@PNC was also better than that of 20 wt% Pt/C at a current density higher than ~50 mA cm^{-2}, although the latter is slightly better at lower current densities. The Tafel slope is another important parameter in studying the reaction pathway and kinetics of electrocatalysts.[43] A systematic investigation was undertaken to probe the catalytic performance across various Ce concentrations (Fig. S15 and S16, ESI†) and dimensional ranges (Fig. S17 and S18, ESI†). The observed size effects may be attributed to variations in surface chemistry or surface electronic structure alterations, influencing the adsorption of intermediates and reaction pathways, thus imposing intrinsic activity dependencies on size. The Tafel slope of WN/WC–CeO_{2-x}@PNC (39.1 mV dec^{-1}) was much lower than that of WN/WC@PNC (140.7 mV dec^{-1}), and lower or comparable slopes as CeO_2 (59.8 mV dec^{-1}), and Pt/C (42.3 mV dec^{-1}) (Fig. 4(b)), indicating that WN/WC–CeO_{2-x}@PNC exhibits fast electrochemical kinetics through the Volmer–Heyrovsky mechanism. The mass activity of WN/WC–CeO_{2-x}@PNC at an overpotential of 200 mV was 7.62 A mg^{-1} (Fig. 4(c)), which far exceeds that of WN/WC@ PNC (3.49 A mg^{-1}) and Pt/C (1.38 A mg^{-1}), indicating the possibility of large-scale industrial applications of the composite catalyst for hydrogen production. Notably, the HER activity of WN/WC–CeO_{2-x}@PNC is better than that of most previously reported TMP-based electrocatalysts (Table S4, ESI†).

The electrochemical impedance spectra of the WN/WC–CeO_{2-x}@PNC and WN/WC@PNC catalysts were acquired in

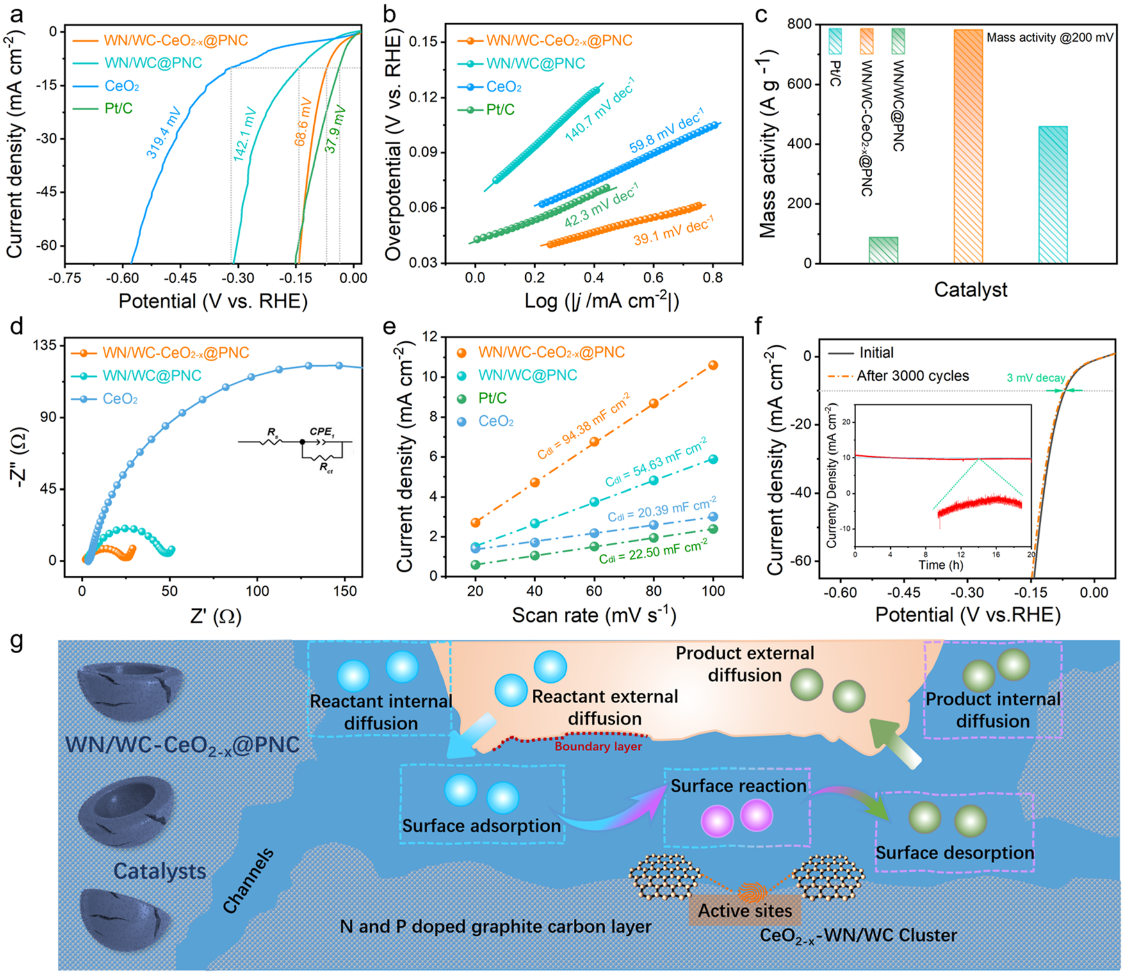

Fig. 4 Evaluation of catalytic activity of developed catalysts for the HER. (a) Polarization curves of all the catalysts for HER. (b) Tafel plots derived from (a) for various catalysts. (c) Mass activity at 200 mV overpotential for WN/WC–CeO_{2-x}@PNC. (d) EIS Nyquist plots of all the catalysts. (e) Plots depicting C_{dl} extraction for various catalysts. (f) Polarization curves of WN/WC–CeO_{2-x}@PNC before and after 3000 CV cycles. Inset: Chronoamperometric curve of WN/WC–CeO_{2-x}@PNC electrode. (g) Schematic of steps affecting the reaction kinetics in WN/WC–CeO_{2-x}@PNC.

1.0 M KOH solution (Fig. 4(d)). The R_{ct} value of WN/WC–CeO_{2-x}@PNC was 22.7 Ω, significantly lower than that of WN/WC@PNC (44.8 Ω) and CeO_2 (312.6 Ω). Thus, compared with the other catalysts, electron transfer is fastest at the electrode/electrolyte interface of CeO_2–WN/WC@PNC. We attribute the fast electron transfer to the three-phase heterogeneous interface containing oxygen defects, and the amorphous region of the unsaturated metal atoms, which can adjust the local charge density of the optimised coordination environment towards the H* species.[44] Secondly, the close vicinity of the core (W–Ce) of the ultra-fine nanoclusters with the N,P-doped carbon shell should further improve the electronic conductivity.[43] To better understand the catalytic mechanism, the electrochemical surface area (ECSA) of the various catalysts was estimated based on the electrochemical double layer capacitance (C_{dl}), which was measured by cyclic voltammetry in the non-faradaic region (Fig. S11, ESI†). The calculated C_{dl} for WN/WC–CeO_{2-x}@PNC (94.38 mF cm^{-2}) is higher than that of WN/WC@PNC (54.63 mF cm^{-2}), CeO_2 (20.39 mF cm^{-2}) and Pt/C (22.50 mF cm^{-2}) (Fig. 4(e)), indicating a larger electrochemical surface area in WN/WC–CeO_{2-x}@PNC, explained by the larger specific surface area, fully exposed clusters, and hierarchical hollow porous structure. In addition to achieving high catalytic activity, another serious challenge for HER electrocatalysts is operational stability, which may prevent large-scale commercialisation. The stability of WN/WC–CeO_{2-x}@PNC during continuous cycling in 1.0 M KOH was studied. In the 20 h chronoamperometric measurement, the current density change is negligible (Fig. 4(f)), and after HER electrocatalysis for 3000 cycles, the LSV curves showed negligible negative shifts compared to those of the fresh catalysts.

Following stability tests, SEM and STEM characterisation (Fig. S12, ESI†) demonstrate a well-preserved morphology and structure of WN/WC–CeO_{2-x}@PNC, in line with the demonstrated good stability. Furthermore, post-durability test XPS analysis and electrolyte ICP-OES testing provide further insights into the catalyst stability and ultra-low leaching, revealing the presence of elements such as W 4f, Ce 3d, N 1s, P 2p, and O 1s, consistent with the expected functionalities (Fig. S13 and Table S3, ESI†). These findings confirm minimal leaching of metal ions and underscore the corrosion resistance of the WN/WC–CeO_{2-x}@PNC electrode in alkaline solutions, particularly in the context of the HER.

The excellent electrocatalytic performance of WN/WC–CeO_{2-x}@PNC can be explained by the variety of favorable structural characteristics at different scales. At the atomic level, the addition of N/P heteroatom can cooperatively change the electronic structure of carbides and improve their intrinsic activity, thereby significantly promoting hydrogen evolution.[43] On the nanometer scale, the hierarchical hollow bowl-like structure of WN/WC–CeO_{2-x}@PNC and fully exposed hetero-clusters are beneficial for promoting mass transport and exposure of rich active centers. From the perspective of catalytic kinetics (Fig. 4(g)), that is, molecular diffusion processes (external and internal diffusion of reactants or products) and surface reaction processes (adsorption, surface reaction and desorption), the hollow nanostructures provide potential opportunities for controllable catalysis by purposefully regulating the diffusion, adsorption and surface reactions of the molecules and intermediates. Moreover, with the generation of intrinsically defective O_{Vs}, the remaining electrons confined to the O_{Vs} flow more easily to the surrounding Ce/W atoms, forming an electron-rich region on the metal atoms.[45,46] More precisely, the delocalised electrons around the metal atoms exhibit stronger attraction of hydrogen and promote the adsorption of hydrogen, thus adding more active sites to the surface of the inert base.

To evaluate the bifunctionality of the catalyst for use in next-generation fuel cells and zinc–air/CO_2 cells, the OER performance was assessed under the same alkaline conditions. Compared with the overpotential of WN/WC@PNC (382 mV), the overpotential and Tafel slope (99.5 mV dec^{-1}) of WN/WC–CeO_{2-x}@PNC, determined from the LSV curve (Fig. S14a, ESI†), were significantly lower (Fig. S14b and d, ESI†). An overpotential of only 286 mV was required to reach a current density of 10 mA m^{-2}. The introduced CeO_2 has redox-active Ce^{4+}/Ce^{3+} pairs (the electronic structure of Ce is [Xe] $4f^15d^16s^2$, where Ce^{3+}

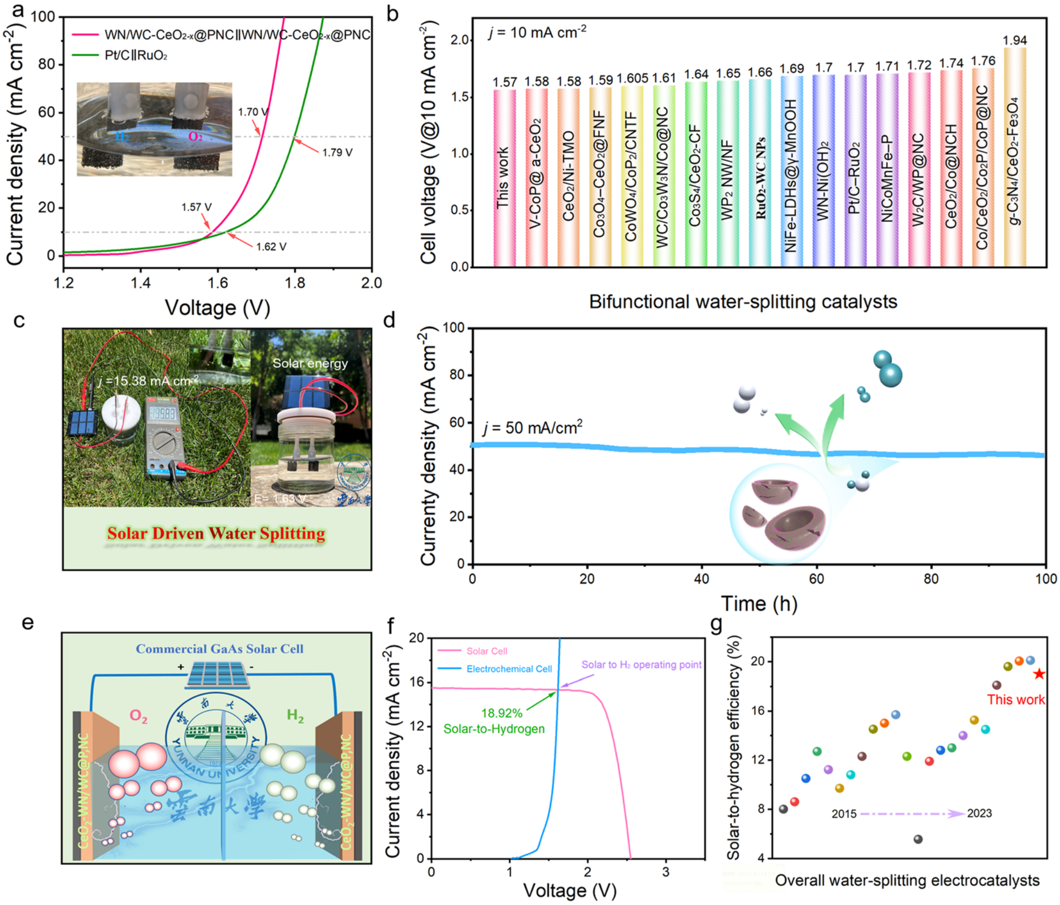

Fig. 5 Solar-driven water splitting configurations and electrochemical performance under actual photovoltaic conditions. (a) Polarization curves of WN/WC–CeO_{2-x}@PNC for overall water splitting. (b) Cell voltages of different electrolysers constructed with bifunctional electrocatalysts for water electrolysis (Table S3, ESI†). (c) Digital photograph of water electrolyser driven by solar cell integrated system. Inset: Photograph of the as-designed two-electrode system confirming the generation of H_2 and O_2 gas bubbles during water electrolysis process. (d) Chronoamperometric stability over 100 h at an applied cell voltage of 1.70 V in alkaline medium (1.0 M KOH). (e) Solar-driven water electrolyser system. (f) Current density *vs.* voltage curve (*J*–*V* curves) of commercially available GaAs-solar cell under AM 1.5G illumination and LSV polarization curve of WN/WC–CeO_{2-x}@PNC for overall water splitting (the operating current density is ~15.38 mA cm^{-2}) (g) Comparison of the solar-to-hydrogen (STH) efficiency achieved in this work with that in the literature (Table S6, ESI†).

and Ce^{4+} are stable and interconvert easily). The abundant lattice oxygen vacancies lead to a significant increase in the OER activity *via* electronic modulation of the active sites.[29] WN/WC–CeO_{2-x}@PNC showed excellent stability after 24 h in the chronoamperometric test, with only a slight decrease in the current density (Fig. S14c, ESI†), attributed to good coupling between CeO_2 and the tungsten-based transition metal compounds, which produced a unique electrocatalyst with enhanced electronic conductivity and structural stability through the synergistic effect.

WN/WC–CeO_{2-x}@PNC was further used as anode and cathode electrocatalysts to evaluate the overall water splitting performance in a two-electrode cell (Fig. 5(a)). For comparison, an electrolytic cell employing commercial RuO_2 and Pt/C as the cathode and anode, respectively, was also tested. The battery voltage with the WN/WC–CeO_{2-x}@PNC electrolytic cell was 1.57 V at 10 mA cm^{-2}, which is better than that obtained with the RuO_2 and Pt/C electrode pairs (1.88 V). The evolution of H_2 and O_2 gas was observed almost instantly upon applying the potential (Fig. 5(a) inset). Notably, the overall hydrolytic performance of this electrolytic cell is better than that achieved with most previously reported non-precious-metal electrocatalysts (Fig. 5(b) and Table S5, ESI†), indicating good potential for practical overall water splitting. In addition, WN/WC–CeO_{2-x}@PNC has excellent durability, after continuous chronopotentiometry measurements at a current density of 50 mA cm^{-2} (Fig. 5(d)) in 1.0 M KOH for 100 h, the electrocatalytic performance decreased negligibly (the small deviation of the current density may be due to continuous bubble formation on the electrode surface, which blocks the active electrode area). This demonstrates that the WN/WC–CeO_{2-x}@PNC have excellent catalytic performance in alkaline conditions, making them highly promising catalysts for energy storage by hydrogen production from solar energy.

Solar-driven water splitting

Given the excellent water splitting performance of the prepared electrocatalyst, a renewable energy conversion system was developed. First, an ordinary 1.5 V solar photovoltaic panel was used to power the hydrolysis process. The combination electrode with the WN/WC–CeO_{2-x}@PNC catalyst produced a large number of hydrogen and oxygen bubbles (Fig. 5(c)), which was closely related to the intensity of the incident sunlight. Thus, the WN/WC–CeO_{2-x}@PNC catalyst is feasible for actual hydrogen production *via* the electrolysis of water. Second, an integrated solar-assisted water decomposition system was designed as a model for hydrogen production from renewable energy sources. Standard GaAs solar cells were connected in series to power the water electrolysis system; the anode and cathode both comprised the WN/WC–CeO_{2-x}@PNC heteroclusters (Fig. 5(e)). H_2 and O_2 bubbles were continuously generated on the surface of the cathode and anode when the integrated system was irradiated with AM 1.5 G (100 mW cm^{-2}) light, indicating that solar energy (photon energy) was effectively converted into H_2 fuel. This also suggests the feasibility of replacing existing photocatalysis and PEC water hydrolysis systems with electrocatalytic water decomposition technology driven by solar cells for hydrogen production. The working current density and the solar-to-hydrogen (STH) conversion efficiency were calculated to further evaluate the solar-assisted water decomposition. From the intersection of the *J–V* curve of the solar cell and the LSV curve of the electrocatalyst in the two-electrode system (Fig. 5(f)), the expected operating current density (J_{op}) of the optoelectronic system of the integrated device at 1.63 V was 15.38 mA cm^{-2}. The STH conversion efficiency was 18.92% (see formula in the Experimental section). The calculated STH values are superior to those of most reported integrated solar water electrolysis systems (Fig. 5(g) and Table S6, ESI†), demonstrating the potential applicability of WN/WC–CeO_{2-x}@PNC in actual solar-driven overall water splitting for hydrogen production. In brief, the integration of the developed electrocatalyst and solar cells enables the system to achieve a stable STH conversion efficiency of 18.92%, which can lay the foundation for achieving more sustainable global energy goals.

Theoretical calculations

In the context of electrocatalytic water splitting, alterations in the energy barriers of the H_2O dissociation and free energy of hydrogen desorption (ΔG_{H^*}) is pivotal for bridging the gap between the theoretical and experimental performance.[47,48] The ΔG_{H^*} for hydrogen adsorption is as a reliable indicator of the catalyst activity. The optimal ΔG_{H^*} should approximate zero to facilitate simultaneous proton adsorption and the release of hydrogen molecules.[2,49] The ΔG_{H^*} values were determined at different atomic positions within the WN/WC@PNC, WN/WC–CeO_2@PNC, and WN/WC–CeO_{2-x}@PNC models (Fig. 6(a)) to evaluate the catalytic activity for the reaction. The W sites of WC within the WN/WC–CeO_{2-x}@PNC catalyst had a ΔG_{H^*} value close to 0 eV, indicating that the oxygen vacancy defects in the vicinity of W positively improves catalytic activity, consistent with the above discussion. This reduced energy barrier can be attributed to modulation of the electronic state of W sites by Ce, resulting in favourable ΔG_{H^*} values and accelerated HER kinetics. The limited number of H^+ ions in alkaline media leads to the inevitable dissociation of H_2O. The adsorption energy of H_2O (ΔE_{H_2O}) on these surfaces was calculated (Fig. 6(b)). The H_2O adsorption energy for WN/WC–CeO_{2-x}@PNC was determined to be −1.02 eV, which is notably lower than that of WN/WC@PNC (−0.39 eV) and WN/WC–CeO_2@PNC (−0.81 eV). This disparity indicates stronger H_2O binding within WN/WC–CeO_{2-x}@PNC, thus ensuring effective water adsorption.

A mechanism for the HER in alkaline electrolytes was proposed, as illustrated in Fig. 6(c). H_2O molecules are initially adsorbed on the W sites near the WN/WC–CeO_{2-x}-V_o@PNC interface. Subsequently, the oxygen vacancies (V_o) in CeO_2 facilitate the dissociation of H_2O into OH* and H*. Hence, this reaction becomes the rate-determining step (RDS), where the generated H* is promptly transferred to and adsorbed on the adjacent Ce–W sites, enabling the subsequent transformation of H to H_2. The synergy between WN/WC and CeO_2 facilitates the adsorption and desorption of reaction intermediates. Remarkably, WN/WC–CeO_{2-x}@PNC exhibited a lower H* desorption energy barrier (0.21 eV) than WN/WC@PNC

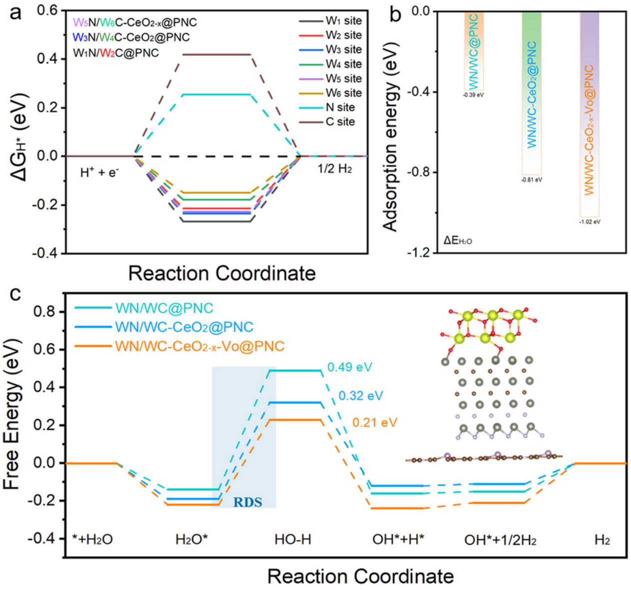

Fig. 6 Theoretical calculation of HER activation energy. (a) Free energy of adsorbed H* intermediates (ΔG_{H^*}) on WN/WC@PNC, WN/WC–CeO_2@PNC, and WN/WC–CeO_{2-x}-V_o@PNC. (b) Adsorption energy for H_2O (ΔE_{H_2O}), and (c) free energy step diagrams for the conversion of H_2O to H_2 on the catalysts.

(0.49 eV) and WN/WC–CeO_2@PNC (0.32 eV), indicating that oxygen vacancies and hetero-clustered WN/WC–CeO_{2-x} disrupt the neutrality of the initial constituents, generating unsaturated atoms and establishing efficient electronic transfer pathways. Ultimately, this orchestrated charge redistribution successfully changes the adsorption energy of the intermediate species in the RDS, thereby catalysing the electrochemical redox reactions.

Conclusions

A design strategy for constructing an active and durable full water-splitting electrocatalyst was developed through spatial confinement of WN/WC–CeO_{2-x} clusters within hollow mesoporous carbon bowls. Compared to conventional tungsten-based nanoparticles, the utilisation of ultrasmall, fully exposed clusters maximise the utilisation of the metal atoms, while providing unique surface and electronic structures. The interface of the WN/WC–CeO_{2-x} hetero-clusters offers abundant electroactive sites, and the three-dimensional porous nanostructure facilitates electron transfer and mass transport. At a current density of 10 mA cm^{-2}, WN/WC–CeO_{2-x}@PNC exhibits overpotentials of 68.6 mV for the HER and 286 mV for the OER, outperforming most previously reported tungsten-based electrocatalysts. Density functional theory calculations revealed that the electronic rearrangement between WN/WC and CeO_{2-x} integrated into the bowl-shaped carbon effectively tuned the local conductivity and charge density. Additionally, the oxygen vacancies and hetero-interface of WN/WC–CeO_{2-x} facilitate water adsorption and disassociation of hydrogen intermediates into H_2 molecules, ultimately expediting the kinetic processes of the HER. This work not only offers insights into the design and synthesis of high-performance catalysts with finely controlled active centres, but also paves the way for advancing existing PEC technologies and carbon-free hydrogen production.

Data availability statement

The data that support the findings of this study are available in the supplementary material of this article.

Author contributions

The manuscript was written with contributions of all authors. All authors have given approval to the final version of the manuscript. Pengliang Sun: conceptualization, investigation, visualization, data curation, writing – original draft, writing – review & editing. Eduardo Gracia-Espino: DFT calculations, writing – review & editing. Fang Tan: Data curation. Hua Zhang: investigation, software. Qingquan Kong: formal analysis and methodology. Thomas Wågberg: check draft, investigation, writing – review & editing. Guangzhi Hu: conceptualization, project administration, supervision, resources, writing – review & editing.

Conflicts of interest

The authors declare no conflict of interest.

Acknowledgements

The authors acknowledge the financial support from This work was financially supported by National Natural Science Foundation of China (U2002213), Science Foundation of Donghai Laboratory (DH-2022KF0314), Open Foundation of Guangxi Key Laboratory of Processing for Non-ferrous Metals and Featured Materials of Guangxi University (2022GXYSOF10), and the Double First-Class University Plan (C176220100042). T. W. acknowledges support from the Swedish Research Council (grant no. 2021-04629).

References

1 T. G. Deutsch, *Nat. Energy*, 2023, **8**, 560–561.
2 J. Guo, Y. Zheng, Z. Hu, C. Zheng, J. Mao, K. Du, M. Jaroniec, S.-Z. Qiao and T. Ling, *Nat. Energy*, 2023, **8**, 264–272.
3 S. Park, L. Liu, Ç. Demirkır, O. van der Heijden, D. Lohse, D. Krug and M. T. M. Koper, *Nat. Chem.*, 2023, **15**, 1532–1540.
4 J. Mo, Y. Ko, Y. S. Yun, J. Huh and J. Cho, *Energy Environ. Sci.*, 2022, **15**, 3815–3829.
5 S. Riyajuddin, M. Pahuja, P. K. Sachdeva, K. Azmi, S. Kumar, M. Afshan, F. Ali, J. Sultana, T. Maruyama, C. Bera and K. Ghosh, *ACS Nano*, 2022, **16**, 4861–4875.
6 J. Wang, G. Ni, W. Liao, K. Liu, J. Chen, F. Liu, Z. Zhang, M. Jia, J. Li, J. Fu, E. Pensa, L. Jiang, Z. Bian, E. Cortes and M. Liu, *Angew. Chem., Int. Ed.*, 2023, **62**, e202217026.
7 R. T. Gao, N. T. Nguyen, T. Nakajima, J. He, X. Liu, X. Zhang, L. Wang and L. Wu, *Sci. Adv.*, 2023, **9**, eade4589.

8 Q. Guo, Q. Zhao, R. Crespo-Otero, D. Di Tommaso, J. Tang, S. D. Dimitrov, M. M. Titirici, X. Li and A. B. Jorge Sobrido, *J. Am. Chem. Soc.*, 2023, **145**, 1686–1695.

9 P. Sun, Y. Zhou, H. Li, H. Zhang, L. Feng, Q. Cao, S. Liu, T. Wågberg and G. Hu, *Appl. Catal., B*, 2022, **310**, 121354.

10 X. Yan, M. Xia, H. Liu, B. Zhang, C. Chang, L. Wang and G. Yang, *Nat. Commun.*, 2023, **14**, 1741.

11 Q. Li, Q. Zhang, W. Xu, R. Zhao, M. Jiang, Y. Gao, W. Zhong, K. Chen, Y. Chen, X. Li and N. Yang, *Adv. Energy Mater.*, 2023, **13**, 2203955.

12 J. Diao, Y. Qiu, S. Liu, W. Wang, K. Chen, H. Li, W. Yuan, Y. Qu and X. Guo, *Adv. Mater.*, 2020, **32**, e1905679.

13 L. K. Brar, A. Gupta and O. P. Pandey, *Catal. Today*, 2019, **325**, 98–108.

14 S. C. Sun, H. Jiang, Z. Y. Chen, Q. Chen, M. Y. Ma, L. Zhen, B. Song and C. Y. Xu, *Angew. Chem., Int. Ed.*, 2022, **61**, e202202519.

15 R. Jamil, R. Ali, S. Loomba, J. Xian, M. Yousaf, K. Khan, B. Shabbir, C. F. McConville, A. Mahmood and N. Mahmood, *Chem. Catal.*, 2021, **1**, 802–854.

16 F. Tan, Y. Zhou, H. Zhang, P. Sun, H. Li, X. Liu, T. Wågberg and G. Hu, *Chem. Eng. J.*, 2023, **454**, 140079.

17 N. Han, K. R. Yang, Z. Lu, Y. Li, W. Xu, T. Gao, Z. Cai, Y. Zhang, V. S. Batista, W. Liu and X. Sun, *Nat. Commun.*, 2018, **9**, 924.

18 H. Yan, C. Tian, L. Wang, A. Wu, M. Meng, L. Zhao and H. Fu, *Angew. Chem., Int. Ed.*, 2015, **54**, 6325–6329.

19 M. Rafei, X. Wu, A. Piñeiro Garcia, V. Miranda la Hera, T. Wågberg and E. Gracia-Espino, *Adv. Mater. Interfaces*, 2022, **9**, 2201214.

20 F. Calle-Vallejo, M. T. M. Koper and A. S. Bandarenka, *Chem. Soc. Rev.*, 2013, **42**, 5210–5230.

21 A. R. Zeradjanin, A. Vimalanandan, G. Polymeros, A. A. Topalov, K. J. J. Mayrhofer and M. Rohwerder, *Phys. Chem. Chem. Phys.*, 2017, **19**, 17019–17027.

22 S. Trasatti, *J. Electroanal. Chem. Interfacial Electrochem.*, 1972, **39**, 163–184.

23 C. Lv, X. Wang, L. Gao, A. Wang, S. Wang, R. Wang, X. Ning, Y. Li, D. W. Boukhvalov, Z. Huang and C. Zhang, *ACS Catal.*, 2020, **10**, 13323–13333.

24 Z. Chen, H. Hu, L. Yin, Z. Zhao, J.-H. Choi, G. Liu and F. Geng, *Proc. Natl. Acad. Sci. U. S. A.*, 2023, **120**, e2209760120.

25 N. Cheng, S. Stambula, D. Wang, M. N. Banis, J. Liu, A. Riese, B. Xiao, R. Li, T. K. Sham, L. M. Liu, G. A. Botton and X. Sun, *Nat. Commun.*, 2016, **7**, 13638.

26 H. Zhang, Z. Bi, P. Sun, A. Chen, T. Wagberg, X. Hu, X. Liu, L. Jiang and G. Hu, *ACS Nano*, 2023, **17**, 16008–16019.

27 X. Liu and L. Dai, *Nat. Rev. Mater.*, 2016, **1**, 1–12.

28 H. Wang, Y. Shao, S. Mei, Y. Lu, M. Zhang, J. K. Sun, K. Matyjaszewski, M. Antonietti and J. Yuan, *Chem. Rev.*, 2020, **120**, 9363–9419.

29 X. Li, X. I. Pereira-Hernandez, Y. Chen, J. Xu, J. Zhao, C. W. Pao, C. Y. Fang, J. Zeng, Y. Wang, B. C. Gates and J. Liu, *Nature*, 2022, **611**, 284–288.

30 S. Wu, Y. Yang, C. Lu, Y. Ma, S. Yuan and G. Qian, *Eur. J. Inorg. Chem.*, 2018, 2944–2951.

31 X. Zheng, Y. Li, L. Zhang, L. Shen, Y. Xiao, Y. Zhang, C. Au and L. Jiang, *Appl. Catal., B*, 2019, **252**, 98–110.

32 J. Kong, Z. Xiang, G. Li and T. An, *Appl. Catal., B*, 2020, **269**, 118755.

33 N. Zhang, Q. Zhang, L. Y. Zhang, J. Y. Zhang, Y. Z. Fang, Z. Liu and M. Zhou, *Small Methods*, 2022, **6**, e2200308.

34 M. Zhang, Q. Dai, H. Zheng, M. Chen and L. Dai, *Adv. Mater.*, 2018, **30**, 1705431.

35 H. F. Wang, L. Chen, H. Pang, S. Kaskel and Q. Xu, *Chem. Soc. Rev.*, 2020, **49**, 1414–1448.

36 D. Li, W. Wan, Z. Wang, H. Wu, S. Wu, T. Jiang, G. Cai, C. Jiang and F. Ren, *Adv. Energy Mater.*, 2022, **12**, 2201913.

37 Y. Zhang, W. Zheng, H. Wu, R. Zhu, Y. Wang, M. Wang, T. Ma, C. Cheng, Z. Zeng and S. Li, *SusMat*, 2023, **4**, 106–115.

38 P. Sun, X. Zheng, A. Chen, G. Zheng, Y. Wu, M. Long, Q. Zhang and Y. Chen, *Adv. Sci.*, 2024, 2309927.

39 P. Sun, S. Liu, X. Zheng, G. Hu, Q. Zhang, X. Liu, G. Zheng and Y. Chen, *Nano Today*, 2024, **55**, 102152.

40 Y. Jiao, Y. Zheng, K. Davey and S.-Z. Qiao, *Nat. Energy*, 2016, **1**, 1–9.

41 Z. Li, J. Li, Z. Zheng, K. Jiang, T. Zheng, D. Wang, H. Wei, Z. Shi, X. Li and H. Chu, *Sci. China: Chem.*, 2022, **65**, 877–884.

42 Y. Liu, C. Ma, Q. Zhang, W. Wang, P. Pan, L. Gu, D. Xu, J. Bao and Z. Dai, *Adv. Mater.*, 2019, **31**, e1900062.

43 J. Liu, X. Yang, F. Si, B. Zhao, X. Xi, L. Wang, J. Zhang, X.-Z. Fu and J.-L. Luo, *Nano Energy*, 2022, **103**, 107753.

44 K. Wang, Y. Guo, Z. Chen, D. Wu, S. Zhang, B. Yang and J. Zhang, *InfoMat*, 2022, **4**, e12251.

45 P. Wang, T. Wang, R. Qin, Z. Pu, C. Zhang, J. Zhu, D. Chen, D. Feng, Z. Kou, S. Mu and J. Wang, *Adv. Energy Mater.*, 2022, **12**, 2103359.

46 S. Jiang, R. Zhang, H. Liu, Y. Rao, Y. Yu, S. Chen, Q. Yue, Y. Zhang and Y. Kang, *J. Am. Chem. Soc.*, 2020, **142**, 6461–6466.

47 S.-P. Zeng, H. Shi, T.-Y. Dai, Y. Liu, Z. Wen, G.-F. Han, T.-H. Wang, W. Zhang, X.-Y. Lang, W.-T. Zheng and Q. Jiang, *Nat. Commun.*, 2023, **14**, 1811.

48 H. Zhang, A. Chen, Z. Bi, X. Wang, X. Liu, Q. Kong, W. Zhang, L. Mai and G. Hu, *ACS Nano*, 2023, **17**, 24070–24079.

49 N. Li, L. Zhang, Y. Wang, S. Zhou, Y. Zhang, A. Abdukayum, Z. Jin, H. Zhang and G. Hu, *J. Colloid Interface Sci.*, 2023, **649**, 125–131.